Monthly Notices of the ROYAL ASTRONOMICAL SOCIETY

MNRAS **508,** 4202–4215 (2021) https://doi.org/10.1093/mnras/stab2673
Advance Access publication 2021 September 20

The GALAH+ survey: a new library of observed stellar spectra improves radial velocities and hints at motions within M67

Tomaž Zwitter [1]★ Janez Kos,[1] Sven Buder [2,3] Klemen Čotar,[1] Martin Asplund,[4] Joss Bland-Hawthorn [3,5] Andrew R. Casey [6,7] Gayandhi M. De Silva,[8,9] Valentina D'Orazi,[10] Ken C. Freeman,[2] Michael R. Hayden,[3,5] Geraint F. Lewis [5] Jane Lin,[2,3] Karin Lind,[11,12] Sarah L. Martell [3,13] Katharine J. Schlesinger,[2] Sanjib Sharma,[5,3] Jeffrey D. Simpson [3,13] Dennis Stello [3,5,13,14] Daniel B. Zucker,[9,15] Kevin L. Beeson,[1] Richard de Grijs,[15,16] Thomas Nordlander [2,3] Yuan-Sen Ting (丁源森),[17,18,19,20] Gregor Traven,[21] Rok Vogrinčič,[1] Fred Watson[22] and Rob Wittenmyer [23]

Affiliations are listed at the end of the paper

Accepted 2021 September 9. Received 2021 August 15; in original form 2021 January 31

ABSTRACT

GALAH+ is a magnitude-limited survey of high-resolution stellar spectra obtained by the HERMES spectrograph at the Australian Astronomical Observatory. Its third data release provides reduced spectra with new derivations of stellar parameters and abundances of 30 chemical elements for 584 015 dwarfs and giants, 88 per cent of them in the *Gaia* magnitude range $11 < G < 14$. Here, we use these improved values of stellar parameters to build a library of observed spectra which is useful to study variations of individual spectral lines with stellar parameters. This and other improvements are used to derive radial velocities with uncertainties which are generally within 0.1 km s^{-1} or ∼25 per cent smaller than in the previous release. Median differences in radial velocities measured here and by the *Gaia* DR2 or *APOGEE* DR16 surveys are smaller than 30 m s^{-1}, a larger offset is present only for *Gaia* measurements of giant stars. We identify 4483 stars with intrinsically variable velocities and 225 stars for which the velocity stays constant over ≥3 visits spanning more than a year. The combination of radial velocities from *GALAH+* with distances and sky plane motions from *Gaia* enables studies of dynamics within streams and clusters. For example, we estimate that the open cluster M67 has a total mass of ∼3300 $M_\odot$ and its outer parts seem to be expanding, though astrometry with a larger time-span than currently available from *Gaia* eDR3 is needed to judge if the latter result is real.

Key words: methods: data analysis – surveys – stars: fundamental parameters – stars: kinematics and dynamics – Galaxy: kinematics and dynamics – open clusters and associations: individual: M67.

1 INTRODUCTION

Galactic archaeology (Freeman & Bland-Hawthorn 2002) aims to decipher the structure and formation of our Galaxy as one of the typical galaxies in the Universe through detailed measurements of stellar kinematics and chemistry of their atmospheres. Recent studies of Galactic dynamics show that the disc is not an axisymmetric equilibrium structure, but dynamically young and perturbed, also by the on-going passages of the Sagittarius dwarf galaxy (Antoja et al. 2018; Helmi et al. 2018; Bland-Hawtorn et al. 2019; Helmi 2020). Such perturbations inflict variations in stellar positions and velocities which are much smaller than their nominal values. Fortunately, astrometric measurements from the second data release of the *Gaia* mission of the European Space Agency (Gaia Collaboration 2018a) provide stellar coordinates, parallaxes, and proper motions with an exquisite accuracy never seen before. The radial velocity (RV) spectrograph on board the same satellite (Cropper et al. 2018) is reporting also the RV measurements for an unprecedented number of over 7 million stars (Katz et al. 2019). While the RV precision for bright stars ($G_{\rm RVS} \in [4, 8]$ mag) is between 0.22 and 0.35 km s^{-1} it worsens to 1.4 km s^{-1} for stars with $G_{\rm RVS} = 11.75$ mag and effective temperature of 5000 K.

Gaia eDR3 proper motion and parallax measurements allow us to measure velocities of stars in the plane of the sky at very high accuracy. For example, a solar type or red clump star at a distance of 1 kpc with a velocity of 9 km s^{-1} (in the plane of the sky) has a *Gaia*-based uncertainty of only ∼0.2 km s^{-1}, and stars moving slower have even smaller uncertainties. Hence, it is desirable to have the perpendicular line-of-sight RVs measured at a similar level of accuracy. Steinmetz et al. (2020) present the final data release of the 10-yr *RAVE* survey. It reports RVs of 518 387 spectra with a typical accuracy of 1.4 km s^{-1}. The *Gaia-ESO* survey (Gilmore et al. 2012) iDR5 lists a smaller number but fainter targets at similar levels of accuracy. The on-going *LAMOST* medium resolution survey

★ E-mail: tomaz.zwitter@fmf.uni-lj.si

(Liu et al. 2020) aims for comparable uncertainty, but for a much larger number of spectra of brighter stars. *APOGEE* DR16 (Jönsson et al. 2020) includes 473 307 spectra, mostly from the Northern hemisphere, with similar precision as reported in this paper (see below). We note that, contrary to our approach, none of these surveys calculates RV taking into account convective shifts within the stellar atmosphere and gravitational redshift of light as it travels to the distant observer.

Here, we describe the derivation of RVs with uncertainties typically smaller than 0.1 km s^{-1}, though for a dozen-times smaller set than derived by *Gaia*. The cornerstone are new values of effective temperature, surface gravity, metallicity, and α-enhancement for 584 015 spectra from the third data release of the *GALAH+* survey (Buder et al. 2021, hereafter B20) which presents also an unprecedented set of measurements of abundances of 30 chemical elements ([X/Fe]) for the same stars. Sharma et al. (2020) and Hayden et al. (2020) show how stellar ages can be inferred for the same objects. Derivation of accurate RVs builds on a procedure described earlier (Zwitter et al. 2018, hereafter Z18), but better parameter values and a number of procedure improvements now make the uncertainties ∼25 per cent smaller, and allow RVs to be derived for 72 per cent more spectra.

The paper is organized as follows: in the next section we briefly discuss the observational data and the reduction pipeline. In Section 3, we present a library of median-combined observed spectra across the stellar parameter space. Section 4 discusses the RV measurement pipeline. Section 5 uses repeated observations of the same stars to identify candidates with constant and with variable RVs. Section 6 illustrates the reach of these results, with a discussion of stellar motions within the cluster M67 used as an example. Section 7 contains the final remarks and Section 8 discusses the data products.

2 OBSERVATIONAL DATA AND THEIR REDUCTIONS

GALAH + includes data from ambitious stellar spectroscopic surveys which use the HERMES spectrograph that simultaneously observes up to 392 stars within the π square degree field of the 3.9-m Anglo-Australian Telescope at the Australian Astronomical Observatory (AAO) at Siding Spring. The surveys are GALAH Phase 1 (bright, main, and faint survey, 70 per cent of all data; De Silva et al. 2015), K2-HERMES (17 per cent; Wittenmyer et al. 2018; Sharma et al. 2019), and TESS-HERMES (5 per cent of data; Sharma et al. 2018), as well as additional GALAH-related projects (8 per cent; Martell et al. 2017), including observations of the bulge and a number of stellar clusters. Spectra cover four wavelength ranges: 4713–4903 Å (blue arm), 5648–5873 Å (green arm), 6478–6737 Å (red arm), and 7585–7887 Å (infrared arm) at a resolving power of $R = 28\,000$. The median S/N per pixel in the green arm is ∼35. For 88.8 per cent of the targets, which are within $G \in [11.0, 14.0]$ mag, this is achieved after three consecutive 20-min exposures, others require shorter or longer sequences. Data from a given star from such an uninterrupted sequence is called a spectrum in this paper. Its effective time of observation is assumed to be mid-time of the sequence.

The data reduction pipeline is described in Kos et al. (2017). We use results of its version 5.3. From the pipeline products, we use the wavelength calibrated spectra in ADU counts (no normalization of continuum) with preserved pixel binning (no resampling). Altogether, 694 459 spectra collected between 2013 November 16 and 2019 February 25 are considered, but with additional requirements on their physical characterization as reported in the third *GALAH+* data release (B20). In particular, we require that the values of effective temperature ($T_{\rm eff}$), surface gravity ($\log g$), [Fe/H], and [α/Fe] are all available in B20. These values are now much more accurate compared with the previous data release (Buder et al. 2018), which translates into a more consistent definition of the observed stellar templates (Section 3) and smaller uncertainties in the RVs (Section 4). Median formal errors are now 98 K in $T_{\rm eff}$, 0.19 dex in $\log g$, 0.088 dex in [Fe/H], and 0.045 dex in [α/Fe]. These error estimates are conservative; table 2 of B20 reports about a third better accuracy at S/N =40. Our final selection contains 579 653 spectra for which RVs are determined. Note that 117 726 of these spectra have the value of reduction flag *flag_sp* >0, indicating problems with spectral peculiarities, data reduction or spectrum analysis. From these 48 638 spectra have astrometric index RUWE >1.4 (these stars may not be consistent with a single-star astrometric solution, Gaia Collaboration 2018a), 18 058 have raised binarity or emission object flags (Traven et al. 2017, 2020), 19 131 have a very low S/N ratio ($S/N < 10$) and others suffer from various reduction or convergence issues. RVs of spectra with *flag_sp* >0 are reported, but they need to be treated with caution.

3 LIBRARY OF OBSERVED SPECTRAL TEMPLATES

Similarly to Z18, we calculate RVs in a two-step process: the observed spectra can be noisy, so we first use a large number of spectra with very similar values of stellar parameters to construct a nearly noise-free observed spectral template which is then compared to synthetic spectra. Such an approach yields better results than direct correlation between observed and synthetic spectra and allows control of systematics, as discussed below. The workflow is similar to the one in Z18, so we do not repeat its description here, but only emphasize the differences.

Spectra are grouped according to values of four parameters: $T_{\rm eff}$, $\log g$, [Fe/H], and [α/Fe]. The alpha abundance is added here because there are a number of scientific applications where a distinction of observed spectra by α enhancement is important. Also, the parameter bins are now different: following the parameter uncertainties mentioned above their values are rounded to the nearest step in the $N\Delta T_{\rm eff}$ ladder in temperature, $N\Delta\log g$ in gravity, $N\Delta$[Fe/H] in iron abundance, and $N\Delta$[α/Fe] in α enhancement, where N is an integer and $\Delta T_{\rm eff} = 200$ K, $\Delta\log g = 0.3$ dex, Δ[Fe/H] = 0.17 dex, and Δ[α/Fe] = 0.09 dex. These rounded values now serve as labels that indicate to which stellar parameter bin our spectrum belongs. Observed spectra are shifted to a common reference frame using RV values from B20 which are accurate to ∼0.4 km s^{-1}, hence better than the Guess values used in Z18.

A meaningful median spectrum can be derived only if we combine a sufficient number of observed spectra within a given parameter bin. We adopt a threshold of 100 spectra per bin, with the additional requirement that they have *flag_sp* =0, thus excluding spectra with peculiarities or reduction problems. There are 718 bins with at least 100 *flag_sp* =0 spectra, so this is also the size of the library of observed spectral templates. The most populous bin is located at the main-sequence turn-off (MSTO; $T_{\rm eff} = 6000$ K, $\log g = 4.2$, [Fe/H] = 0.0, [α/Fe] = 0.0) and contains 7290 spectra, from these 6315 have *flag_sp* = 0.

The spectra are interpolated to a log-spaced grid which is ∼3-times denser than the observed one (122 88 points over each of the 4713–4900, 5468–5871, 6478–6736, 7693–7885Å intervals). Next, they are normalized with a three-piece cubic spline with symmetric 3.5 σ rejection levels and 10 iterations. The combined spectrum is calculated as a weighted median of spectra, with weights proportional

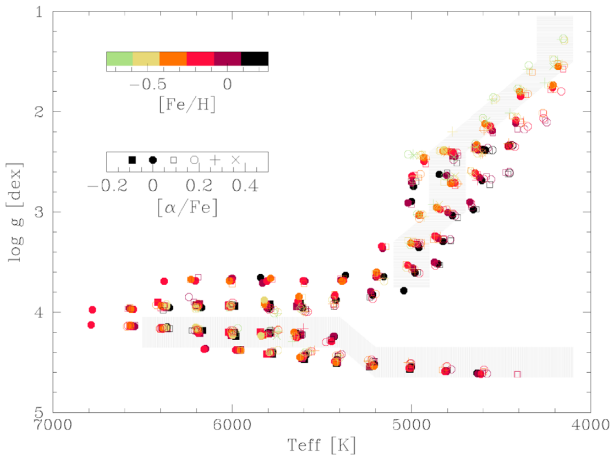

Figure 1. Kiel diagram of a library of observed median spectra. Their iron abundances are colour coded and different symbols mark the α-enhancement bins, as indicated in the legend. Medians in grey areas along the main sequence and the red giant branch are used for plotting of equivalent widths of spectral lines in Figs 3–8.

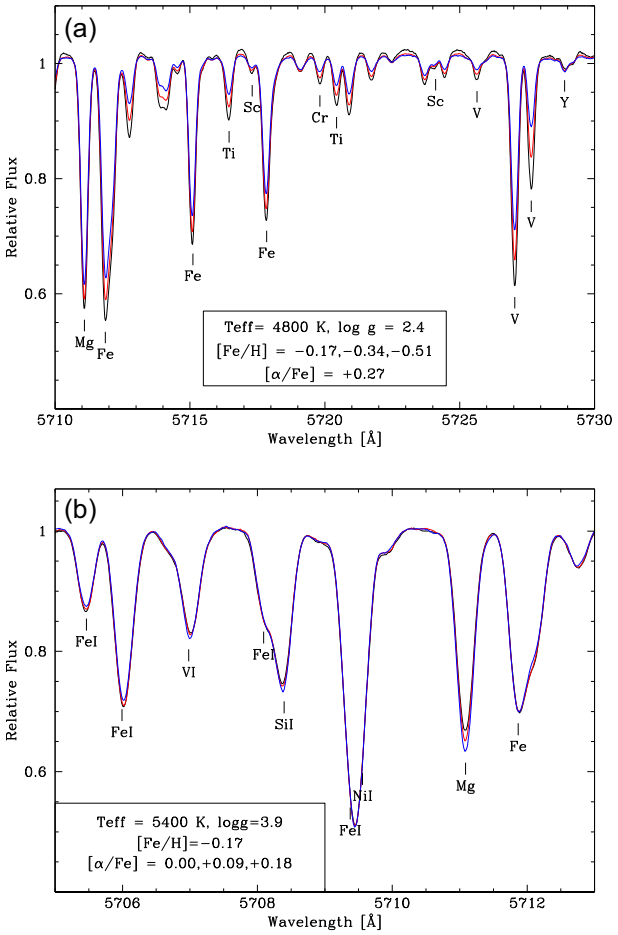

Figure 2. A sequence of median observed spectra in the green arm, varying their iron abundance (a) or α-enhancement (b).

to the square of the S/N ratio in the red channel, truncated at S/N =200. This is a better choice than a simple median used in Z18. However, such a weighted median could potentially be driven by a small number of very high S/N spectra in a given parameter bin; we checked that this is not the case.

Fig. 1 plots the 718 spectral bins in a Kiel diagram. The position of each bin is given as a weighted median of $T_{\rm eff}$ and $\log g$ values of its spectra. So the symbols with colour-coded iron abundances and α-enhancements plotted with different symbols do not overlap completely. The figure demonstrates a good coverage of stellar evolutionary tracks, with the exception of hot or very cool stars, which are rarely observed by *GALAH*.

Fig. 2 shows two series of observed median spectra if all but one parameter is kept constant. Panel (a) shows how spectra change with [Fe/H], and panel (b) demonstrates a variation with [α/Fe]. Understandably, the former affects the depth of all spectral lines, while the latter shows variation mostly in lines of α elements. A moderately different continuum level of spectra in panel *a* is due to normalization process: we use symmetric rejection criteria so the continuum is at a level a bit larger than 1.0, depending on the strength of absorption lines. Note that even when [Fe/H] is kept constant (panel b), the strengths of the Fe lines vary slightly because of slight differences in mean $T_{\rm eff}$ and [Fe/H] between the different [α/Fe] groups.

A library of observed spectral templates can have different uses. An example is the measurement of equivalent widths (EWs) of individual spectral lines. This can be tricky in individual observed spectra, as noise does not allow an unambiguous placement of the continuum level. The situation with spectral medians is different, as they are nearly noise-free. Figs 3–8 show EWs of the strongest unblended lines of 30 chemical elements measured by *GALAH*, arranged by their atomic number *Z*. Reported EWs are calculated over a line mask range, with the continuum set to the maximum value within the segment mask range for each line (see table A3 in B20). In each figure, the top panel shows EWs along the main sequence (MS) and the bottom one along the RGB, defined by grey bands in Fig. 1. Iron abundances are colour-coded and α enhancements are presented with different symbols. As expected, iron group elements have all symbols (different [α/Fe]) with a given colour (a given [Fe/H]) overlapping, with a monotonic relation between EW and [Fe/H]. Since [X/H] correlates with [Fe/H] this explains correlations of lines that are not from the iron group. On the other hand EWs of α elements, especially along the RGB, have non-overlapping symbols of a given colour (different [α/Fe] at the same [Fe/H]). The behaviour of some elements is entirely different, such as Li I 6708, C I 6588, and O I 7772 (Fig. 3); Si I 5684 (Fig. 4); Cu I 5782 and Zn I 4811 (Fig. 6); Ba II 6497 (Fig. 7); and Sm II 4792 (Fig. 8). Discussion of individual cases is beyond the scope of this paper. These graphs demonstrate the well-known fact that the strength of spectral lines can serve as a sensitive stellar thermometer, and that medians of observed spectra present an interesting overview of spectral changes across the HR diagram.

4 RV MEASUREMENT PIPELINE

As a first step we compute RV shifts of each observed spectrum versus the relevant observed median spectrum. This is done as in Z18, using an iterative process of computing a weighted average of 20 wavelength intervals along the four spectrograph arms. Next, we need to compute the RV shift between the observed median spectrum and a suitable synthetic spectral library. We use the one of Chiavassa et al. (2018), which includes 3D convective motions within the stellar atmosphere. It has been computed using the radiative transfer code Optim3D (Chiavassa et al. 2009) for the STAGGER grid of 3D radiative hydrodynamical simulations of stellar convection (Magic

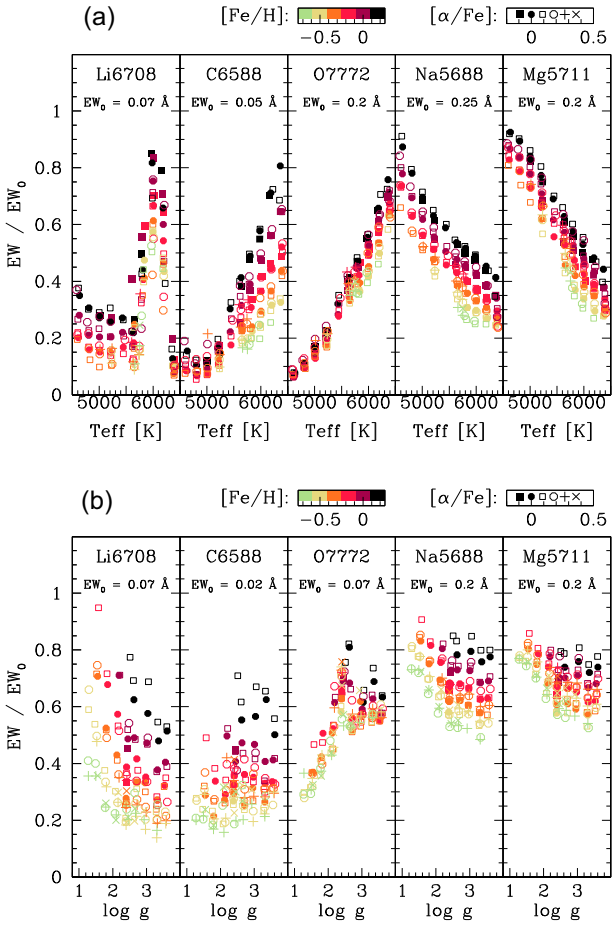

Figure 3. Equivalent widths of the strongest lines of elements with $3 \leq Z \leq 12$ along the main sequence (a) and the red giant branch (b). Iron abundances are colour coded, different symbols mark the α-enhancement bins, as indicated in the legend.

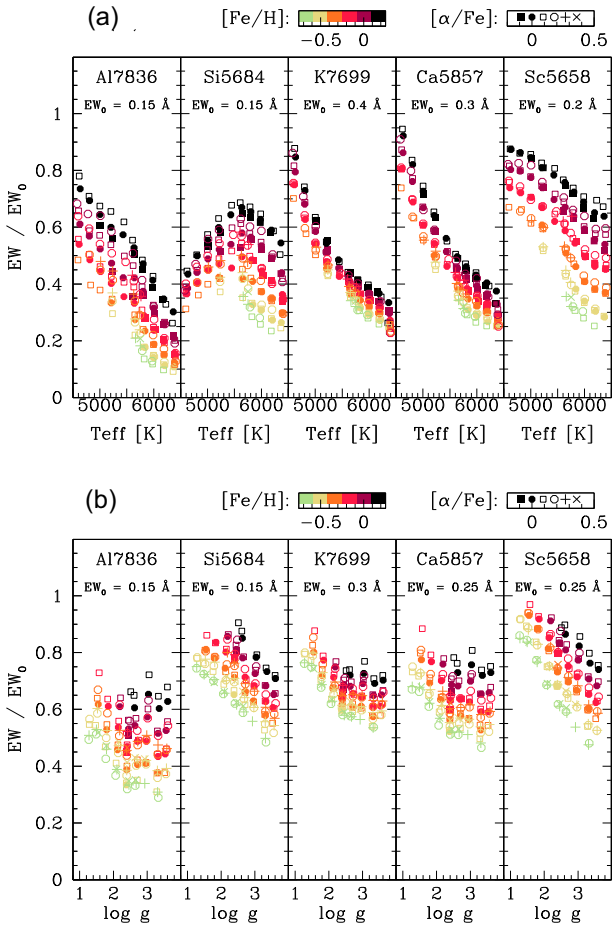

Figure 4. As Fig. 3, but for lines of chemical elements with $13 \leq Z \leq 21$.

et al. 2013). The convective motions give rise to convective blueshifts which vary from line to line, depending on line strengths, element, ionization stage, excitation potential etc. (see e.g. Asplund et al. 2000, for the Sun). These are accounted for in the Chiavassa et al. 3D synthetic spectra which should improve the RV determinations.

Comparison of observed median spectra to synthetic ones can yield more than one RV measurement. In particular, one expects that RVs measured over different wavelength intervals of a given spectrum are consistent within errors. If they are not and if deviations in a given wavelength region are seen over a range of spectral types this indicates a problem with the wavelength calibration of this region. This can be due to a lack of suitable ThAr calibration lines with accurately known wavelengths or a result of PSF variation, which is typical for fast focal-ratio spectrographs, including HERMES (Kos et al. 2018).

The RV calculation can be sensitive to a moderately different chemical composition of the observed median and synthetic spectra. So we first renormalize both spectra in each arm of the spectrograph using a 3-piece cubic spline with asymmetric rejection (low_rej =3.0, high_rej =5.0) and 10 iterations. To detect any systematic RV shifts we divide the spectral range of each arm into 20 fine intervals with a width of 10–14 Å. This gives us 80 RV measurement points over 718 observed median templates. Fig. 9 shows that some systematic shifts are present. We use 85 median templates which are based on the largest numbers of combined observed spectra and have $T_{\rm eff} \leq$ 6000 K. We then compare their RV within a given wavelength bin to a peak of a combined correlation function of all wavelength bins and over all 4 arms of the spectrograph. In an ideal case we would expect a random scatter around zero. Fig. 9 shows that some wavelength bins have large error bars because they do not contain any strong spectral lines. Some points also show large offsets, which reflect a mismatch between synthetic and observed spectra or a presence of a strong not fully matched spectral line at the edge of the wavelength bin. All this is expected. But Fig. 9 also shows that for example the red edges of the green, red and IR arms have residuals with consistently negative sign, indicating a systematic blueshift.

The continuous curves in Fig. 9 are derived as running weighted averages of individual points, penalizing their wavelength distance by a Gaussian with $\sigma = 500$ km s^{-1}. This value was chosen to mimic a typical density of ThAr lines and an expected spatial variation of the PSF within the spectrograph. These curves are used as corrections to shift the RVs from the individual wavelength bins, which would help us deriving more consistent RVs of the observed median spectra. In particular, the typical RV uncertainties reported by Z18 were 0.09 km s^{-1}. The use of better values for the stellar parameters, the use of [α/Fe] values for constructing the median observed spectra, a larger number of RV bins and a better implementation of the correlation routine now allows us to bring this down to 0.042 km s^{-1}. Finally, taking the just mentioned wavelength correction into account reduces the uncertainty to 0.027 km s^{-1}.

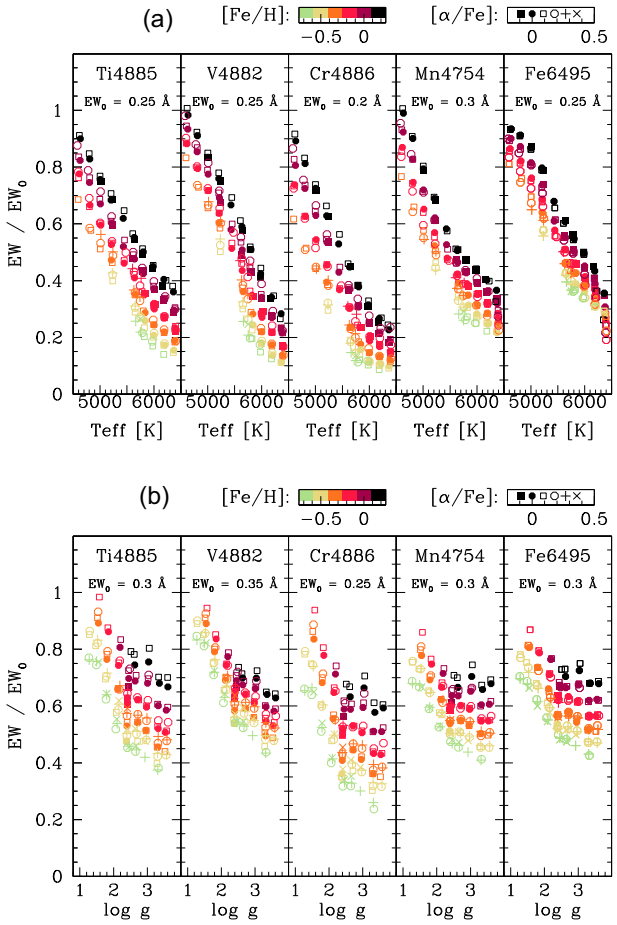

Figure 5. As Fig. 3, but for lines of chemical elements with $22 \leq Z \leq 26$.

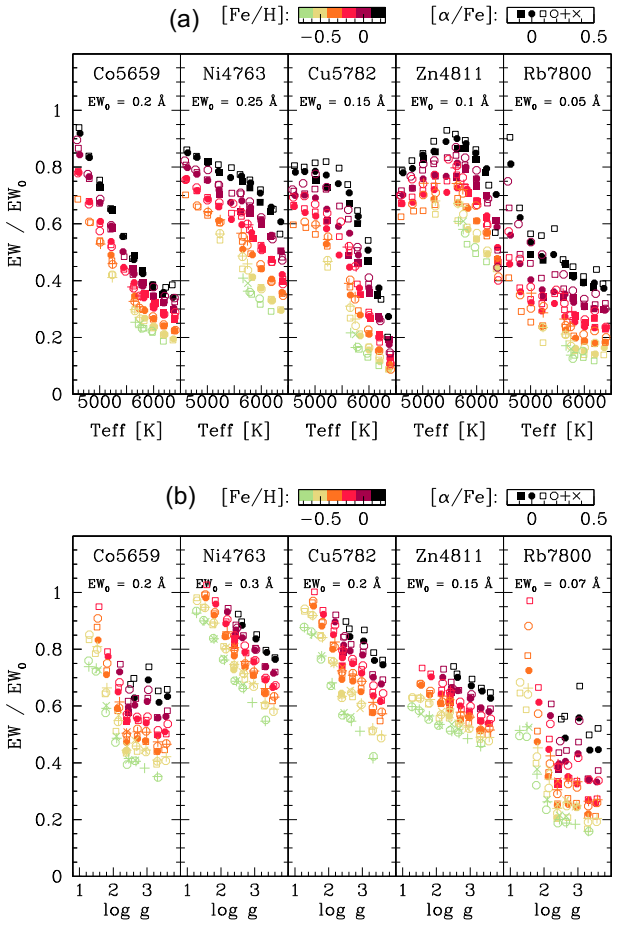

Figure 6. As Fig. 3, but for lines of chemical elements with $27 \leq Z \leq 37$.

A meaningful calculation of median spectra requires well populated bins in the ($T_{\rm eff}$, $\log g$, [Fe/H], [α/Fe]) space. As discussed above there are 718 such bins, each with at least 100 un-flagged spectra. Together they contain 474 309 spectra, the other 106k spectra belong to less populous bins. For the less populous bins we use the median observed spectra from the closest well populated bin. That bin is determined as the one with the smallest Manhattan distance $\frac{\Delta T_{\rm eff}}{a} + \frac{\Delta \log g}{b} + \frac{\Delta[{\rm Fe/H}]}{c} + \frac{\Delta[\alpha/{\rm Fe}]}{d}$, with $(a, b, c, d) = (2\,{\rm K}, 0.01\,{\rm dex}, 0.1\,{\rm dex}, 0.4\,{\rm dex})$. This choice of constants, which was found by trial and error to pick the most similar rescaled spectrum, reflects the fact that spectra change quickly with temperature, less with gravity, while chemistry mostly reflects only the depth of (certain) lines and thus has a minor influence on derived RVs.

To complete the RV calculation we need to consider two final steps. The first one is a barycentric correction. Here, it is done with the routine *bcvcorr*, which is part of the *IRAF* RVSAO package and is more accurate than *rvcorr* used in Z18. Next, we note that light suffers from gravitational redshift as it travels from the stellar surface to the observer. This effect is substantial, it reaches 0.636 km s^{-1} for a solar type star and is proportional to the ratio of the stellar mass and radius. So stars of different types would show inconsistent RVs if this effect was neglected.

The implementation of gravitation redshift is the same as described in Z18, but benefits from better values of the stellar parameters. Still, one should note that the radius of the star is difficult to determine accurately. So the final velocities, which take gravitational redshift into account, are internally consistent but have substantially larger uncertainties than without taking gravitational redshift into account. So one should use values corrected for gravitational redshift if different types of stars are to be compared, such as within a stellar cluster or in studies of Galactic dynamics. But if the goal is to study RV variability of a certain star, the values without gravitational redshift correction are preferred because of the more realistic uncertainties. Also, most stars can be regarded as static in our sample. However, we measure the stellar parameters for each spectrum separately even when multiple spectra per star are available, which may induce some variation in calculation of gravitational redshifts. Finally, most of the published catalogues, including RVs from *Gaia*, do not include gravitational redshift corrections at present. So in general, one needs to use our values without gravitational redshift correction to compare them to the ones from the literature. As explained below we therefore publish RVs with and without gravitational redshift correction.

Fig. 10 plots cumulative distributions of uncertainties for RVs with and without gravitational redshift correction, separately for dwarfs and giants (the dwarf-giant separation line is defined in eq. 1 in Z18). The uncertainties were derived using a strict error propagation, as explained in Z18. The values are now ∼25 per cent smaller, mostly due to more accurate stellar parameters, a better wavelength calibration, and other computational improvements, as explained above. The gravitational redshift correction increases the uncertainties, because there are uncertainties in the determination of the stellar parameters that need to be factored in. Values for

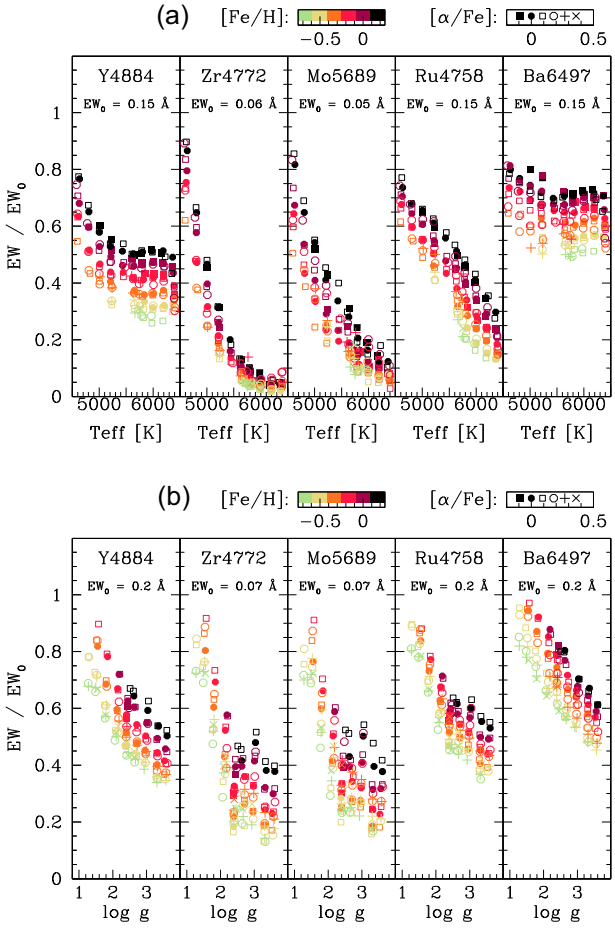

Figure 7. As Fig. 3, but for lines of chemical elements with $39 \leq Z \leq 56$.

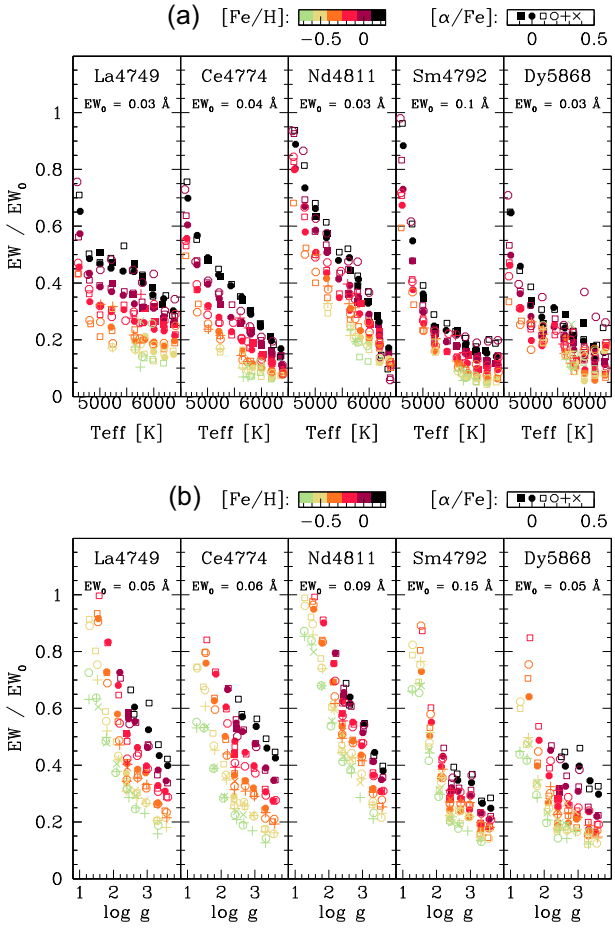

Figure 8. As Fig. 3, but for lines of chemical elements with $57 \leq Z \leq 66$.

giants are better than for dwarfs, which reflects the abundance of spectral lines and smaller importance of the gravitational redshift correction for giants compared to dwarfs. We see that the majority of uncertainties, especially when considering measurements without the gravitational redshift correction, are within 0.1 km s^{-1}.

Table 1 reports results of the RV measurement pipeline. The whole table is available electronically.

5 OBJECTS WITH VARIABLE AND WITH CONSTANT RVS

GALAH+ is mostly a single visit survey. But 25 358 stars have more than one spectrum satisfying flag_sp =0 and have RVs measured by our procedure. From these 21 379 have a pair of observations, 2784 have 3 visits, 676 have 4 visits, 203 have 5 visits, 139 have 6 visits, 125 have 7 visits, 51 have 8 visits, and one star has been observed 9 times. Such a statistics of repeated observations is not enough to study properties of stars with variable RVs or to determine if a star has a stable RV over a long term. Still, with a suitably stringent selection criterion, we can identify candidates with intrinsically variable RVs and candidates with constant RVs. In both cases we use the RVs without gravitational redshift correction, as this correction would inflate the RV error bar due to uncertainties in the values of the stellar parameters.

To quantify the significance of RV differences between two measurements with assumed Gaussian distributions (RV$_1$, σ_1) and (RV$_2$, σ_2) one can write the probability P that a random pick from the second distribution is larger than the one from the first one:

$$P = \frac{1}{2\pi\sigma_1\sigma_2}\int_{-\infty}^{\infty}\int_{-\infty}^{y} \times \exp\frac{-(x-\mathrm{RV}_1)^2}{2\sigma_1^2}\exp\frac{-(y-\mathrm{RV}_2)^2}{2\sigma_2^2}\mathrm{d}x\mathrm{d}y \quad (1)$$

which can be simplified to (Matijevič et al. 2011)

$$P = \frac{1}{2}\left[1+\mathrm{erf}\left(\frac{|\mathrm{RV}_1-\mathrm{RV}_2|}{\sqrt{2(\sigma_1^2+\sigma_2^2)}}\right)\right] \quad (2)$$

where erf is the standard error function. For two measurements with nearly matching RVs this probability is close to 1/2, but for an object with a significant RV variation the value will converge to 1. If we use a 4 σ type of criterion for the detection of RV variability, hence $P > 0.9999366575$, we find 4483 stars with variable RV. From these 2592 are MS objects (defined as in Z18). Intrinsically variable stars are listed in Table 2 to be published in full in electronic form at the CDS.

In most cases the number of RV observations is too small to derive a solution of the RV curve. But, as said, there are 177 stars with 7 or more observations. For example, the star 2MASS 04071697 − 6301357 ≡ Gaia DR2 4676308341177919744 has 7 observations spanning a RV range of 123.487 km s^{-1} (Table 2). A circular solution $\mathrm{RV} = K \sin 2\pi\frac{t-t_0}{P} + \gamma$, with K = 65.36(1) km s^{-1}, P = 3.3488673(28) days, γ = 9.233(1) km s^{-1},

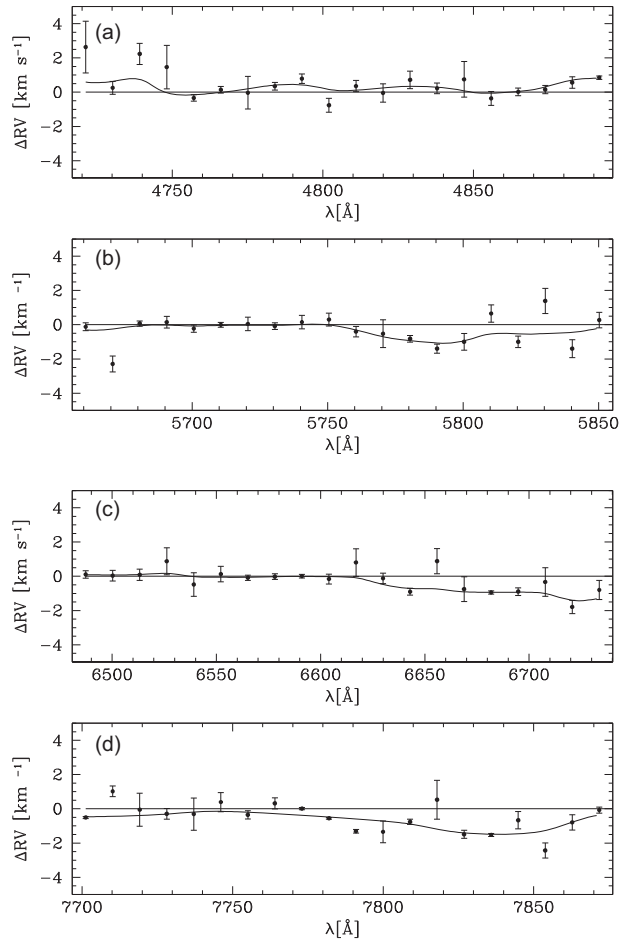

Figure 9. Correction to a wavelength solution as derived from a piecewise comparison of observed median spectra and synthetic templates. ΔRV is the difference between a weighted average of median observed spectra and the overall RV, which is defined as a peak of a combined correlation function of all wavelength bins and over all arms of the spectrograph.

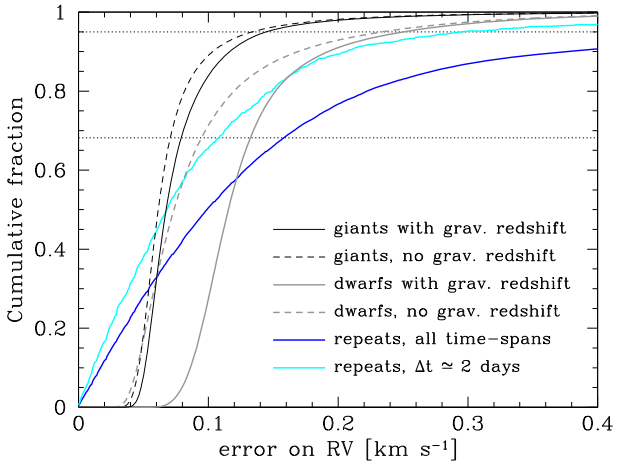

Figure 10. Cumulative histogram of formal radial velocity uncertainties for giants (black) and dwarfs (grey) with (full line) an without (dashed line) gravitational redshift correction. Coloured curves are cumulative distributions of standard deviation of actual repeated RV measurements of the same objects re-observed 2 d apart (cyan) or at any time-span (blue). Horizontal dotted lines mark the 68.2 per cent and 95 per cent levels.

$BJD(t_0) = 2457571.1256(2)$, fits the observations with $\overline{O-C} = 0.339$ km s^{-1}. Its mass function equals $0.0969 M_\odot/\sin^3 i$ and is consistent with a low mass secondary component. The star has not been studied so far, except by the *2MASS* (Cutri et al. 2003) and *Gaia* (Gaia Collaboration 2021b) surveys. *Gaia* reports a large uncertainty of mean RV, which is compatible with our results.

Another important use of repeated observations is to establish which stars have a constant RV and can therefore serve as RV standards. *GALAH+* generally observes fainter stars than listed in published catalogues of RV standards. But the number of *GALAH* observations is generally too small and their time-span too short to firmly establish them as RV standards. Still, we can build a list of candidates, which can be used for validation of other surveys, though with a caveat that some of the targets may eventually turn out to have a variable RV. Table 3 lists 225 objects with at least three observations which span more than a year in time and less than 0.2 km s^{-1} in their individual RV measurements (without gravitational correction).

Repeated observation can be used to verify the precision of the derived RVs. The blue curve in Fig. 10 is a cumulative histogram of all pairs of measurements of the same objects at all time-spans. Note that many of these objects are intrinsically variable, as discussed above. So the cyan curve shows results for repeated observations obtained 2 days apart, which should filter out any long-term variability. It shows that 68.2 per cent of the pairs of measurements are within ±0.109 km s^{-1}. Use of other short time-spans yields similar results. The exception is observation within the same night or in consecutive nights, which have typical uncertainties of ±0.127 km s^{-1}. In such cases the second observation was often obtained because of an unsatisfactory quality of the first one.

Table 1. All RVs presented in this paper forming a Value added catalogue of RVs of *GALAH+* DR3. The velocity columns list the RV and its uncertainty for measurements including the gravitational redshift (RV) and for those without this correction (RV_nogr). MJD is the local modified Julian date, and JD the heliocentric Julian date. A complete list is published electronically.

sobject_id	2MASS_id	Gaia_DR2_id	RV km s^{-1}	RV_nogr km s^{-1}	MJD (local)	JD (heliocentric)
131116000501002	03325271-6840304	4667368899326729856	36.204 ± 0.183	36.890 ± 0.138	56612.5155509	2456613.01580
131116000501004	03422255-6841522	4667324643983679744	95.878 ± 0.151	95.914 ± 0.150	56612.5155509	2456613.01579
131116000501005	03373408-6841062	4667335913977929728	7.130 ± 0.126	7.565 ± 0.096	56612.5155509	2456613.01579
131116000501006	03430488-6843208	4667323681911007232	24.816 ± 0.163	25.349 ± 0.159	56612.5155509	2456613.01579
131116000501007	03425716-6844462	4667323544472053888	-38.360 ± 0.136	-37.917 ± 0.099	56612.5155509	2456613.01579
...	...	...	...	...	...	...

Table 2. Stars with variable RVs that exceed a 100 km s^{-1} amplitude. N is number of observations. The last four columns give details of the pair of measurements with the largest RV difference. A complete list of 4483 stars with variable RV at a 4 σ level is available electronically.

2MASS_id	Gaia_DR2_id	N	$\lvert RV_2 - RV_1 \rvert$ (km s^{-1})	$t_2 - t_1$ (d)	sobject_id$_1$	sobject_id$_2$
09541851-6939098	5243109471519822720	2	196.756	737.98624	151225004301112	180101005001112
10015471-4131014	5418823008865449472	2	147.292	237.37062	170507006201267	171230006301071
05203528 + 0120357	3234152606303000576	3	123.536	3.02859	190209002401182	190212002001182
04071697-6301357	4676308341177919744	7	123.487	246.31468	170107001801301	170910005601301
07050942-6724015	5280932808950813824	2	122.571	710.89050	170110002101048	181222003601047
04111667-6739489	4668410652234512256	4	112.460	0.91227	171207002701149	171208001601149
06152332-6159006	5481076085919696640	2	105.065	2.84710	170203001901305	170206002901305
06475902-3407140	5582458995101542656	2	104.242	1393.17875	140312001701146	180103003101146
...	...		...	...	...	...

Table 3. Stars with constant RVs with at least $N \geq 3$ observations that span $\Delta t \geq 1$ yr in time and ΔRV < 0.2 km s^{-1} in their individual RV_nogr measurements. The last two columns list the weighted average RV and its uncertainty for measurements including the gravitational redshift (RV) and for those without this correction (RV_nogr). A complete list of 225 stars with constant RVs is available electronically.

2MASS_id	Gaia_DR2_id	N	ΔRV (km s^{-1})	Δt (d)	RV (km s^{-1})	RV_nogr (km s^{-1})
04062738-6252547	4676358403316733696	8	0.170	1476.82127	37.108 ± 0.053	37.458 ± 0.049
04111980-7051077	4654280897025535360	4	0.044	506.65084	10.582 ± 0.055	10.997 ± 0.047
12044223-3949215	3459350489096016640	4	0.047	441.75844	24.948 ± 0.024	25.002 ± 0.024
12061470-3944312	3459344132544717824	4	0.110	443.79997	61.912 ± 0.054	61.969 ± 0.054
12051308-4010565	3458953393599646336	4	0.146	443.79996	14.260 ± 0.059	14.299 ± 0.057
12064427-4009095	6149476076392742144	4	0.159	441.81152	67.091 ± 0.069	67.609 ± 0.063
08233294-1919135	5707436496101210624	4	0.160	387.00457	33.492 ± 0.090	34.120 ± 0.064
04111504-7139337	4653848406703013760	4	0.163	831.78819	–5.834 ± 0.079	–5.272 ± 0.068
04094116-6317034	4676286621527513344	4	0.166	384.94644	–6.122 ± 0.070	–5.500 ± 0.063
12035022-3947097	3459023762343865984	4	0.184	441.75841	59.808 ± 0.062	59.912 ± 0.063
04120308-6114296	4676931386313930496	4	0.198	1476.85275	75.390 ± 0.098	75.493 ± 0.093
...	...		...	...	...	...

6 MOTIONS WITHIN M67

A combination of *Gaia* astrometry and our RVs allows us to study the 3D position and velocity vectors of stars *within* stellar streams or clusters. Here we use the open cluster M 67 as an example. The same approach can be expanded to other clusters and associations.

We selected M 67, as *GALAH+* observed 244 of its members listed in Carrera et al. (2019, hereafter C19). Its age is 3.64 Gyr (Bossini et al. 2019), with recent estimates ranging from 3.46 Gyr (Stello et al. 2016) to 4.2 Gyr (Barnes et al. 2016), so its stars do not show signs of activity typical for young objects, which may otherwise complicate RV determinations. Its old age means it can be assumed to be dynamically relaxed from its birth motions. Its distance is typical for stars observed by *GALAH* (the median parallaxes of *GALAH* stars is 1.18 mas), so the results can be similar for other streams or associations.

GALAH+ observed only a quarter of the cluster's members, so general properties of M 67 need to be adopted from the literature. We assume the cluster's centre is at $\alpha_c = 132.84595^{\rm o}$, $\delta_c = 11.813988^{\rm o}$ (epoch 2016.0), its proper motion is $\mu_{\alpha c} = -10.986$ mas yr^{-1}, $\mu_{\delta c} = -2.964$ mas yr^{-1}, and the distance to the cluster centre is $d_c = 860$ pc (Cantat-Gaudin et al. 2018).

Next, we define the coordinate system. A star at a distance d, with equatorial coordinates (α, δ), proper motions (μ_α, μ_δ) and radial velocity RV can have its position written in Cartesian coordinates as $d(\cos\delta\cos\alpha, \cos\delta\sin\alpha, \sin\delta)$. For convenience we translate and rotate this system, so that it is centred on M67, has its z axis pointing away from Earth, while the x an y axes are tangential to the celestial sphere and pointing to the east and north, respectively. The position of the star $\vec{r} = (x, y, z)$ now becomes

$$\begin{aligned} x &= d\cos\delta\sin(\alpha - \alpha_c) \\ y &= d[\sin\delta\cos\delta_c - \cos\delta\sin\delta_c\cos(\alpha - \alpha_c)] \\ z &= d[\sin\delta\sin\delta_c + \cos\delta\cos\delta_c\cos(\alpha - \alpha_c)] - d_c \end{aligned} \quad (3)$$

and its velocity vector $\vec{v} = (\dot{x}, \dot{y}, \dot{z})$ with respect to the centre of the cluster is

$$\begin{aligned} \dot{x} &= \mathrm{RV}\cos\delta\sin(\alpha - \alpha_c) - d\mu_\delta\sin\delta\sin(\alpha - \alpha_c) \\ &\quad + d\cos(\alpha - \alpha_c)(\mu_\alpha - \mu_{\alpha c}\cos\delta/\cos\delta_c) \\ \dot{y} &= \mathrm{RV}[\sin\delta\cos\delta_c - \cos\delta\sin\delta_c\cos(\alpha - \alpha_c)] \\ &\quad + d\sin\delta\sin\delta_c[\mu_\delta\cos(\alpha - \alpha_c) - \mu_{\delta c}] \\ &\quad + d\cos\delta\cos\delta_c[\mu_\delta - \mu_{\delta c}\cos(\alpha - \alpha_c)] \\ &\quad + d\sin\delta_c\sin(\alpha - \alpha_c)[\mu_\alpha - \mu_{\alpha c}\cos\delta/\cos\delta_c] \\ \dot{z} &= \mathrm{RV}[\cos\delta\cos\delta_c\cos(\alpha - \alpha_c) + \sin\delta\sin\delta_c] - \mathrm{RV}_c \\ &\quad + d\sin\delta\cos\delta_c[-\mu_\delta\cos(\alpha - \alpha_c) + \mu_{\delta c}] \\ &\quad + d\cos\delta\sin\delta_c[\mu_\delta - \mu_{\delta c}\cos(\alpha - \alpha_c)] \\ &\quad + d\cos\delta_c\sin(\alpha - \alpha_c)[-\mu_\alpha + \mu_{\alpha c}\cos\delta/\cos\delta_c] \end{aligned} \quad (4)$$

where RV_c is the RV of the cluster centre. These Cartesian coordinates are co-moving with the cluster centre ($\vec{r}_c = \vec{v}_c = 0$), so they correct for perspective effects (van de Ven et al. 2006).

For further study we select 193 stars that are not in binary systems (according to the classification by C19), have $T_{\rm eff} < 6150$ K (thus avoiding blue stragglers), have their parallaxes and proper motions published in Gaia Collaboration (2021b) and which have all their RV measurements within 3 km s^{-1} of the RV_c (faster stars are probably unbound, unrelated to the cluster, or have intrinsically variable RVs). The value of RV_c was determined iteratively from our measurements so that the median of $\dot{z}$ is zero, yielding $RV_c = +33.927 \pm 0.054$ km s^{-1}. We always use RV values with a gravitational redshift correction, because only these yield consistent values for different stellar types. This result is similar to Geller, Latham & Mathieu (2015) who derive the cluster's RV as +33.64 km s^{-1} from a much larger sample of RV measurements but neglecting convective and gravitational shifts. C19 classifies 9 of our stars as members of the red clump (RC), 25 as red giant branch (RGB) stars, 18 as subgiants (SGB), 65 as MSTO, and 76 as MS stars. B20 uses isochrone fitting to estimate their masses m. The values span the range between 0.77 and 1.71 $M_\odot$, in agreement with a very flat mass function of M 67 (Hurley et al. 2005).

The position of the stars on the sky plane is known very well, but their distance has a larger uncertainty. The median uncertainty in the parallax of the cluster members, as listed by *Gaia* eDR3, is 19.3μas, which at the distance of M 67 translates to 14.3 pc. The astrometric precision of *Gaia* is truly fantastic and unprecedented, but typical distance uncertainties are still comparable to the size of the cluster (∼15 pc), as determined by Gaia Collaboration (2018b). So we cannot use a simple inversion of the parallax to determine the distance of a star. Note that use of a general Galactic prior (Bailer-Jones et al. 2018) is not appropriate due to a different space distribution of cluster members. We adopt a Nuker surface density profile (van der Marel & Anderson 2010), with coefficients as derived by C19, and invert it into a spherically symmetric radial probability distribution of cluster stars. This probability distribution is then sampled along the line-of-sight column of each of our stars. Such a procedure can determine a distribution of possible distances for each star which is then sampled with 10 000 realizations, discarding outliers with a distance difference to the cluster centre larger than 17 pc (an approximate limiting radius of the cluster, Gao 2018). Similarly, we use reported uncertainties to sample RVs and proper motion values (taking their correlations into account) and determine a distribution of the 3D space coordinates and velocity vectors for each star. Individual realizations of the velocity vector for a given star have a small average spread ($\sigma_{\dot{x}} = 0.08$ km s^{-1}, $\sigma_{\dot{y}} = 0.06$ km s^{-1}, $\sigma_{\dot{z}} = 0.12$ km s^{-1}), the same is true for the x and y coordinates ($\sigma_x = 0.008$ pc, $\sigma_y = 0.008$ pc), while the spread in z ($\sigma_z = 3.47$ pc) is much larger, though smaller than what would be obtained from a simple parallax inversion.

Fig. 11(a) plots the x and y position and velocity of each star observed by *GALAH*+. The z position is more uncertain, so we indicate its value by using filled symbols for stars close to the xy plane and open ones for the stars away from it. The latter are stars which have $z^2 > x^2 + y^2$ for at least half of their realizations. The $\dot{x}$ and $\dot{y}$ components are shown with a line with a length of 1 pc for each 2 km s^{-1}, and the $\dot{z}$ component is indicated by the colour of the symbol. The figure demonstrates that we observed many stars in the central part of the cluster, while those at large distances are mostly offset to negative y values, i.e. in the southern direction. This is understandable, as stars with large northern declinations are difficult to observe from the *GALAH*'s southern observing site.

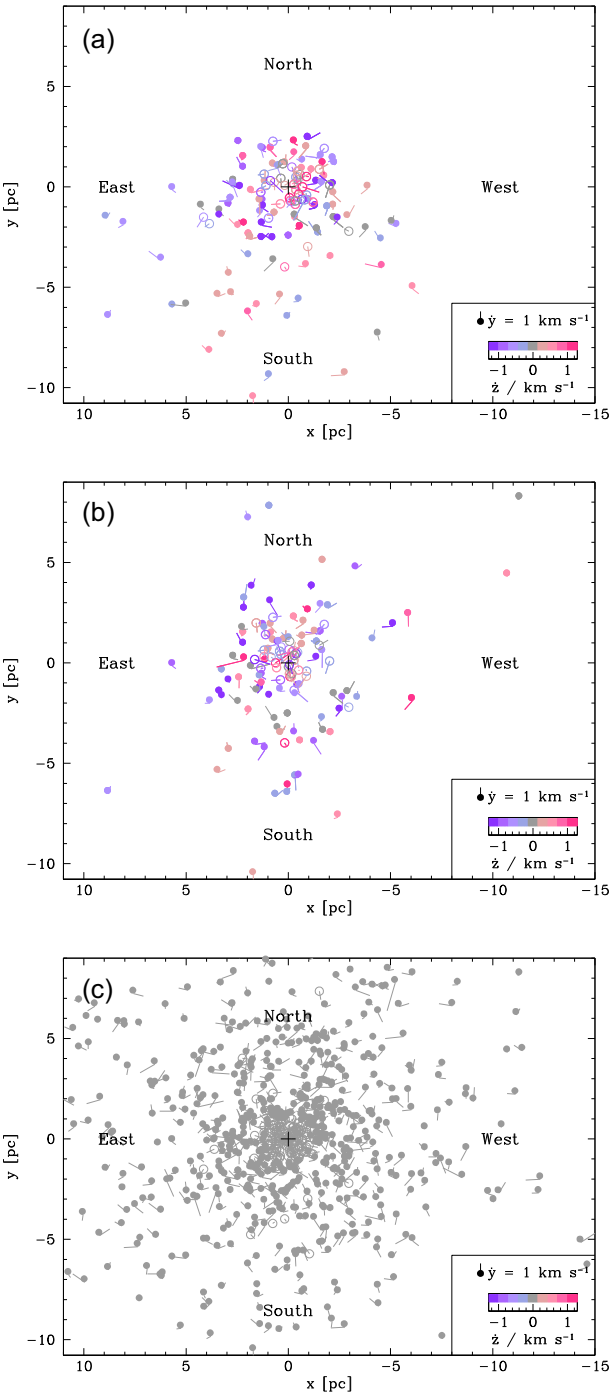

Figure 11. Positions and velocity vectors of single stars in M 67 that were observed by *GALAH*+ (a), by *APOGEE* DR16 (b), and by *Gaia* eDR3 (c). In the latter case all RVs were assumed to be equal to RV_c. The position of each star is marked with a dot with a colour indicating its $\dot{z}$ velocity, and the line indicating its $\dot{x}$ and $\dot{y}$ velocities with a length of 0.5 pc corresponding to 1 km s^{-1}. Filled symbols mark stars close to the xy plane, and open symbols the ones which are away from it. The black plus sign marks the cluster centre.

Spreads around the cluster centre in the x, y, and z directions are 1.96, 1.75, and 2.93 pc, respectively. The latter value is largely driven by the assumed Nuker density profile.

Asymmetric spatial distribution of stars observed by *GALAH* may influence the results on their motion with respect to the cluster

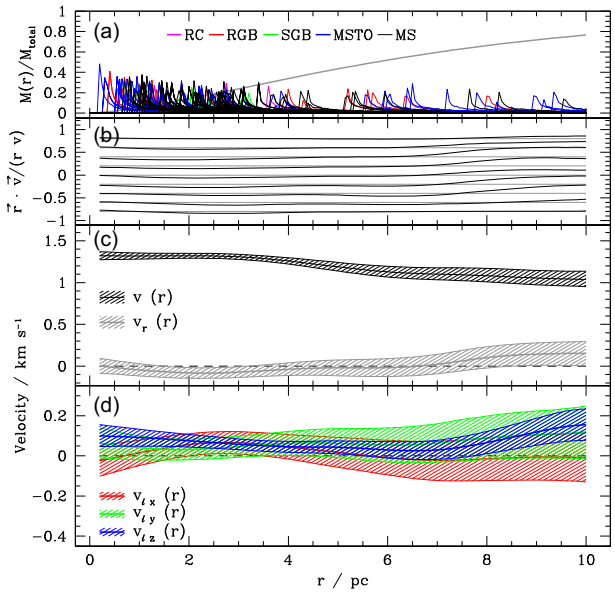

Figure 12. Large scale motions of stars within M67 and observed by *GALAH+* as a function of distance from the cluster centre. Panel (a) presents distributions of possible positions for each of the observed stars on an arbitrary scale and the mass fraction from the adopted Nuker density profile (in grey). Panel (b) shows the distribution of the cosine of the angle between the vectors $\vec{v}$ and $\vec{r}$. The lines depict the angle at 10, 20,..., 90 per cent of the distribution: thin grey lines are for an isotropic distribution which has a flat distribution of cosine values between −1 and 1, and thick black lines are for the actual observed distribution. Panel (c) plots the size of the velocity vector ($v(r)$, black) and its projection to the radial direction ($v_r(r)$, grey), while panel (d) shows the three components of the angular velocities ($v_{\ell x}$: red, $v_{\ell y}$: green, $v_{\ell z}$: blue). Thick lines in panels (c) and (d) are the median values and the shaded regions show the 16 per cent to 84 per cent level spread, as derived from 10 000 realizations of position and velocity of the each of the 193 observed stars. Results in panels b-d are smoothed with a Gaussian with $\sigma = 1$ pc. Zero values in panels (c) and (d) are indicated by a dashed line.

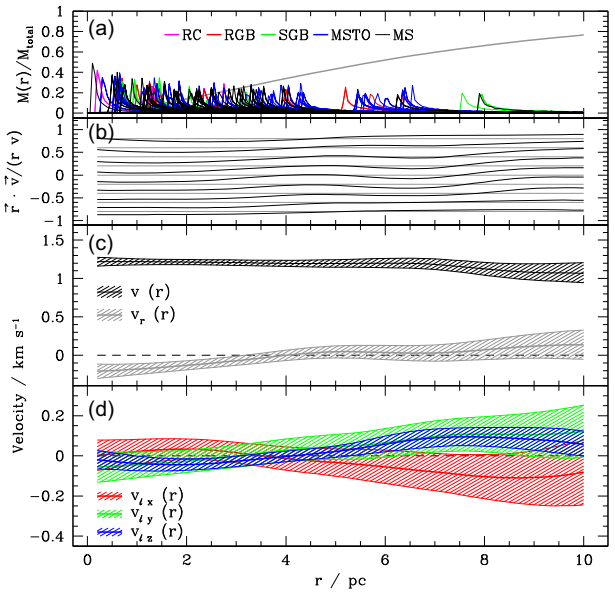

Figure 13. As Fig. 12, but for stars observed by *APOGEE* DR16 with their RVs modified, so that they include the effect of gravitational redshift. See the text for details.

centre. So we include two independent data sets from the literature. *APOGEE* DR16 (Jönsson et al. 2020) lists observations of 213 stars satisfying the selection criteria discussed above. Their RVs have errors similar to *GALAH*, but they do not include gravitational redshift. So we added this effect (see Section 4) using the values of stellar parameters derived by *APOGEE*. *Gaia* eDR3 presents astrometric measurements of a complete sample of 808 cluster members which are single stars, but only 62 of these stars have their RVs measured by *Gaia* and with an average error of 1.3 km s^{-1}. So we decided to use a complete sample but with the assumption that all stars have their RVs equal to RV$_c$. Note that such fixing of one of the components of the velocity vector damps any large scale motions observed within the cluster. Panels 11(b) and (c) plot positions and velocities for the *APOGEE* and *Gaia* samples.

Fig. 11 presents accurate information on individual velocity vectors and on two out of three spatial coordinates for each of the observed stars. So it is interesting to check if this picture includes some ordered large scale motions within the cluster. Fig. 12 presents results for the *GALAH DR3+* sample, while Fig. 13 is its equivalent for RVs measured by *APOGEE*. Each figure has four panels we discuss next.

Panel 12(a) illustrates probability distributions of radial positions for each of the stars. The distributions are colour-coded by spectral type of the star, as determined by C19 and confirmed by stellar parameters reported in B20. Each probability distribution has a sharp peak at a minimal distance r from the cluster centre which is permitted by the x and y coordinates of the star, because the density profile favours small absolute values of z. In cases where the parallax value indicates a position in front of or behind the cluster the distribution has a long tail to larger values of r. The same panel plots also the mass fraction as a function of radius, as given by the adopted Nuker profile. The function is convex at small radii, but this high density region contains only a small fraction of the total mass. Further out the mass fraction is approximately proportional to the distance, and at $r > 6$ pc it turns to a moderately concave shape, as it includes most of the cluster mass.

Panel 12(b) examines the angle between the vectors $\vec{v}$ and $\vec{r}$. It plots the cosine of this angle which has a uniform distribution in the isotropic case. This property is illustrated by uniformly spaced thin grey lines which show the cosine values at 10, 20,..., 90 per cent of the distribution. However, the thick black lines show the same information, but for the actual observed stars. These lines, and all the other curves in the next panels, are actual values for all realizations of all observed stars, but smoothed with a Gaussian with $\sigma = 1$ pc. Such a choice presents a suitable averaging of individual measurements, yet it preserves the general trends with distance from the cluster centre.

Directions of the velocity vectors in Fig. 12(b) are close to isotropic at all radii. So the stars are generally not in circular orbits. This is demonstrated also by the grey line in Fig. 12(c), which plots the median value of the radial component of the velocity vector $v_r(r) = \vec{v} \cdot \vec{r}/r$, with the shaded region between 16 and 84 percentiles. Similarly, the black line and its shadowed region in Fig. 12(c) show the size of the velocity vector $v(r)$.

Subtracting the two curves one can estimate the total mass of the cluster: $M_{\rm total} = r\frac{v^2(r)-v_r^2(r)}{G}[\frac{M(r)}{M_{\rm total}}]^{-1}$, where the last term is given by the adopted Nuker density profile. For the region with $M(r)/M_{\rm total} > 0.5$, corresponding to $r > 5.73$ pc, we get $M_{\rm total} = 3300 \pm 100$ M$_\odot$. There are three reasons why we need to exclude stars close to the cluster centre when estimating the total mass of the cluster: (i) for these stars the uncertainty of the z coordinate increases the fractional uncertainty of their r coordinate, (ii) $M(r) \ll M_{\rm total}$ for these stars, so

any error in the adopted density profile strongly affects the derived value of the total mass, and (iii) many of the stars in the inner parts of the cluster are close to periastrons of their elliptical orbits, so their velocities are larger than for stars on circular orbits. In particular, the velocity curve $v(r)$ does not decrease towards zero as we approach the cluster centre. Numerical integration of orbits adopting a stationary Nuker density profile and ignoring any star-star encounters allows us to estimate their typical eccentricities and orbital periods. For the same outer region we obtain eccentricities $\epsilon \equiv \frac{r_{max}-r_{min}}{r_{max}+r_{min}} = 0.5 \pm 0.2$, with their distribution approximately following a sine-like curve between 0 and 1. So typical stars are on rather elliptical orbits, with $\frac{r_{max}}{r_{min}} \equiv \frac{1+\epsilon}{1-\epsilon} \sim 3$, with the median orbital period of the radial motion of 88 Myr. Stars which stay closer to the cluster centre have shorter orbital periods, as $M(r) \propto r$. The fact that the orbits are not circular is clear already from the directions of the velocity vectors in Fig. 11. The elliptical shape of the stellar orbits may be the reason for the rather large size of the cluster of ∼16 pc (Gaia Collaboration 2018b; Gao 2018).

Orbits in the cluster are not symmetrical, but the inferred radial component of the velocity vector is small compared to $v(r)$, with absolute values between 0.1 and 0.2 km s^{-1}. Similarly, Fig. 12(d) is used to illustrate if stars located away from the cluster core show any net rotation. By writing the angular momentum $\vec{\ell}(r) = m\,\vec{r} \times \vec{v} = mr\vec{v}_\ell$ we can plot the components of the angular velocity $\vec{v}_\ell = (v_{\ell x}, v_{\ell y}, v_{\ell z})$. Note that all these quantities are assumed to depend only on the distance from the cluster centre (r), in agreement with the spherically symmetric nature of the Nuker density profile.

Significance of any large scale motions can be judged by comparing results of different surveys which also observe different sets of stars. Fig. 13 does so using RVs measured by the *APOGEE* survey. Results are compatible with *GALAH+*. In both cases the significance of non-zero values of $v_r(r)$ and $\vec{v}_\ell$ is generally at a one sigma level. Moreover, these results use *Gaia* eDR3 astrometry which may suffer from spatially correlated systematic errors for objects with angular separations less than one degree, thus relevant for M 67. Vasiliev & Baumgardt (2021) show that this introduces a lower limit on the uncertainty of parallaxes and proper motions at the level of 0.01 mas and 0.025 mas yr^{-1}, respectively. Parallax errors of M 67 stars quoted by *Gaia* eDR3 are about twice as large, so effects of systematics are moderate. On the other hand, reported errors on proper motions have an average of 0.023 and 0.015 mas yr^{-1} for right ascension and declination, respectively. So they may be affected significantly by the possible systematics, which is a consequence of a limited number of scans collected by *Gaia* over the first 34 months of the mission.

To address these concerns we tried to quantify contributions of individual types of measurements to the inferred large scale motions in M 67. Appendix A presents results which are equivalent to Fig. 12 but obtained by omission of different types of measurements: by applying the cluster average proper motion or RV to all targets, or assuming that their velocities are isotropic. These tests show that RV measurements by *GALAH+* and *APOGEE* hint at a radial expansion of the outer parts of the cluster. Evidence for a possible large-scale rotation is even more uncertain.

All results on large scale motions have a low statistical significance, largely because of possible systematics affecting the proper motion measurements. This is bound to change with the next data releases of *Gaia* which will not be affected by the scanning law even for sources at small angular separations. Nevertheless, expansion and rotation of the outer parts of M 67, if confirmed by improved future astrometry, is not unexpected. Despite its large age, the cluster may not be completely relaxed. This has been suggested before. C19 find a number of stars belonging to an extended halo of M 67.

Table 4. Difference in RV between the *GALAH+* measurements without the gravitational redshift correction presented here and the corresponding values measured by the *Gaia* DR2 (Gaia Collaboration 2018a) and the *APOGEE* DR16 (Jönsson et al. 2020) surveys. Measurements of the latter survey come in three variants: average RV (HRV), average RV from observed template technique (HRV2), and average RV from synthetic spectrum template matching technique (HRVs). Only objects with flag_sp =0 (B20) are considered. The dwarf-giant separation line is defined in eq. 1 in Z18. The scatter is half of the difference between the 84.1 and 15.9 percentile levels, calculated after an iterative 3σ clipping.

Survey	Spectral type	Spectra in common	ΔRV (km s^{-1}) Median	Scatter
Gaia	dwarfs	93 793	+0.009	1.344
	giants	110 468	−0.122	0.761
APOGEE(HRV)	dwarfs	5422	+0.024	0.376
	giants	6520	−0.027	0.308
APOGEE(HRV2)	dwarfs	5426	+0.015	0.366
	giants	6522	−0.027	0.302
APOGEE(HRVs)	dwarfs	5425	+0.033	0.367
	giants	6521	−0.021	0.303

They explain their presence by relatively frequent passages of the cluster through the Galactic plane, the last one only ∼40 Myr ago. Hurley et al. (2005) use an N-body simulation to show that the cluster lost ∼90 per cent of its initial mass during its evolution. The halo members were not observed by *GALAH*, but here we see a tidal excitation in motions of stars within the cluster. The stars are moving in highly eccentric orbits which may explain the large size of the cluster. These stars are gravitationally bound and given their median period of radial motion of 88 Myr (and its large spread) we note that the last passage through the galactic disc occurred about half of the orbital period ago. As noted by C19 the cluster passed the Galactic disc three times in the last 200 Myr. These perturbations keep the cluster in an excited state, so that it did not have enough time yet for a dynamical relaxation.

7 CONCLUSIONS

In this paper we presented the construction of a new library of observed median spectra observed by the *GALAH+* survey, based on parameters of its DR3 data release (B20). As an example of its use we measured EWs of strong spectral lines of 30 chemical elements across the HR diagram. The observed median spectra are virtually noise-free so that their RVs versus synthetic spectra can be computed over many wavelength intervals which may contain only weak lines. This means that any mismatches in the strength of spectral lines which result from synthetic grid limitations are less important, while moderate displacements of spectral lines which persist over a wide range of median spectra can be used to improve the wavelength solution. The new library and a number of procedure improvements allowed a computation of more accurate RVs of more stars than available before. Altogether we list RVs for 579 653 spectra of 548 056 different stars, with formal velocity uncertainties that are generally smaller than 0.1 km s^{-1}. These RVs come in two versions: the values with the gravitational redshift correction are to be used for dynamical studies and when radial velocities of different types of stars are to be compared. The values without the gravitational redshift correction have smaller uncertainties and are useful for studying RV variability or when comparing *GALAH* RVs with other surveys, which generally do not include this correction. As an example, Table 4 compares RVs derived here with the *Gaia*

DR2 and the *APOGEE* DR16 measurements. Median differences are between 9 and 33 m s^{-1}, with an opposite sign of the difference for dwarfs and giants. The only exception are *Gaia* DR2 measurements of giant stars where our RVs are ∼120 m s^{-1} smaller than derived by *Gaia*. Considering that these surveys do not have their zero points calibrated on each other, we find these results very satisfactory.

Accurate RVs find their use in detailed studies of Galactic dynamics, which show that our Galactic home is not an ordered equilibrium system, but includes a number of complex oscillations, see a recent demonstration by Gaia Collaboration (2021a). It seems that this applies also to motions of stars *within* stellar clusters. In particular, *GALAH+* observed 244 members of the open cluster M 67 and determined their RVs. We used *Gaia* eDR3 astrometry to construct a probabilistic 3D map of positions of these stars within the cluster. By adding RVs we also determined their velocity vectors with respect to the centre of the cluster. The size of the velocity vector is consistent with a total mass of the cluster of 3300 ± 100 M$_\odot$. Stars are in elliptical orbits, typical eccentricity is 0.5 ± 0.2.

We realize that the cluster is not at rest, with some hints of expansion and rotation in its outer parts, though these claims have a low statistical significance. The situation is expected to be clarified when current RV measurements from *GALAH+* and *APOGEE* surveys will be combined with future data releases of *Gaia* that will be free from systematics which may currently affect astrometry of compact sources, such as stars in clusters. To the best of our knowledge this is the first such kinematic study of an open cluster. It is a witness to the accuracy achievable with *Gaia* astrometry when combined with accurate radial velocities. A similar analysis can be done also for some other stellar clusters and for stellar streams across the Galaxy.

ACKNOWLEDGEMENTS

We thank the referee for very useful comments on the manuscript. Based on data acquired through the Australian Astronomical Observatory, under programmes: A/2013B/13 (The *GALAH* pilot survey); A/2014A/25, A/2015A/19, A2017A/18 (The *GALAH* survey phase 1), A2018 A/18 (Open clusters with HERMES), A2019A/1 (Hierarchical star formation in Ori OB1), A2019A/15 (The *GALAH* survey phase 2), A/2015B/19, A/2016A/22, A/2016B/10, A/2017B/16, A/2018B/15 (The HERMES-TESS program), and A/2015A/3, A/2015B/1, A/2015B/19, A/2016A/22, A/2016B/12, A/2017A/14 (The HERMES K2-follow-up program). We acknowledge the traditional owners of the land on which the AAT stands, the Gamilaraay people, and pay our respects to elders past and present. TZ, JK, and KČ acknowledge financial support of the Slovenian Research Agency (research core funding No. P1-0188) and the European Space Agency (Prodex Experiment Arrangement No. C4000127986). Parts of this research were supported by the Australian Research Council Centre of Excellence for All Sky Astrophysics in 3 Dimensions (ASTRO 3D), through project number CE170100013.

This work has made use of data from the European Space Agency (ESA) mission *Gaia* (http://www.cosmos.esa.int/gaia), processed by the *Gaia* Data Processing and Analysis Consortium (DPAC, http://www.cosmos.esa.int/web/gaia/dpac/consortium). Funding for the DPAC has been provided by national institutions, in particular the institutions participating in the Gaia Multilateral Agreement.

The following software and programming languages made this research possible: IRAF (Tody 1986, 1993), SUPERMONGO (version 2.4.43, developed by Rober Lupton and Patricia Monger); TOPCAT (version4.4, Taylor 2005); PYTHON and its packages ASTROPY (Astropy Collaboration et al. 2013), SCIPY (Jones et al. 2001), MATPLOTLIB (Hunter 2007), and NUMPY (Walt, Colbert & Varoquaux 2011). This research has made use of the VizieR catalogue access tool, CDS, Strasbourg, France (Ochsenbein, Bauer & Marcout 2000).

DATA AVAILABILITY

This paper has two main data products. A library of median observed stellar spectra can be downloaded from the *GALAH* DR3 website, as explained in B20. Similarly, the radial velocity catalogue with and without gravitational redshift corrections can be downloaded as one of the Value Added Catalogues from the same website. All observed median spectra and all tables are available also from the first author's homepage.[1] Complete versions of Tables 1–3 are available online and from the CDS Vizier service.

REFERENCES

Antoja T. et al., 2018, Nature, 561, 360
Asplund M. et al., 2000, A&A, 359, 729
Astropy Collaboration, 2013, A&A, 558, A33
Bailer-Jones C. A. L. et al., 2018, AJ, 156, 58
Barnes S. A. et al., 2016, ApJ, 823, 16
Bland-Hawthorn J. et al., 2019, MNRAS, 486, 1167
Bossini D. et al., 2019, A&A, 623, A108
Buder S. et al., 2018, MNRAS, 478, 4513
Buder S. et al., 2021, MNRAS, 506, 150(B20)
Cantat-Gaudin T. et al., 2018, A&A, 618, A93
Carrera R. et al., 2019, A&A, 627, A119 (C19)
Chiavassa A. et al., 2009, A&A, 506, 1351
Chiavassa A. et al., 2018, A&A, 611, 11
Cropper M. et al., 2018, A&A, 616, A5
Cutri R. M. et al., 2003, The IRSA 2MASS All-Sky Point Source Catalog, NASA/IPAC Infrared Science Archive.
De Silva G. M. et al., 2015, MNRAS, 449, 2604
Freeman K., Bland-Hawthorn J., 2002, ARA&A, 40, 487
Gaia Collaboration, 2018a, A&A, 616, A1
Gaia Collaboration, 2018b, A&A, 616, A10
Gaia Collaboration, 2021a, A&A, 649, A8
Gaia Collaboration, 2021b, A&A, 649, A1 (Gaia eDR3)
Gao X., 2018, ApJ, 869, 9
Geller A. M., Latham D. W., Mathieu R. D., 2015, AJ, 150, 97
Gilmore G. et al., 2012, Msngr, 147, 25
Hayden M. R. et al., 2020,(arXiv:2011:13745)
Helmi A., 2020, ARA&A, 58, 205
Helmi A. et al., 2018, Nature, 563, 85
Hunter J. D., 2007, Comput. Sci. Eng., 9, 90
Hurley J. R. et al., 2005, MNRAS, 363, 293
Jones E., Oliphant T., Peterson P. et al., 2001, SciPy: Open source scientific tools for Python. http://www.scipy.org/
Jönsson H. et al., 2020, AJ, 160, 120
Katz D. et al., 2019, A&A, 622, A205
Kos J. et al., 2017, MNRAS, 464, 1259
Kos J. et al., 2018, MNRAS, 480, 5475
Liu C. et al., 2020, preprint (arXiv:2005.07210)
Magic Z. et al., 2013, A&A, 557, A26
Martell S. L. et al., 2017, MNRAS, 465, 3203
Matijevič G. et al., 2011, AJ, 141, 200
Ochsenbein F., Bauer P., Marcout J., 2000, A&AS, 143, 23
Sharma S. et al., 2018, MNRAS, 473, 2004
Sharma S. et al., 2019, MNRAS, 490, 5335
Sharma S. et al., 2020, preprint (arXiv:2011.13818)
Steinmetz M. et al., 2020, AJ, 160, 82
Stello D. et al., 2016, ApJ, 832, 133

[1] http://fiz.fmf.uni-lj.si/zwitter/GALAHDR3/

Taylor M. B., 2005, in Shopbell P., Britton M., Ebert R., eds, ASP Conf. Ser. Vol. 347, Astronomical Data Analysis Software and Systems XIV. Astron. Soc. Pac., San Francisco, p. 29
Tody D., 1986, in Crawford D. L., ed., Proc. SPIE Conf. Ser. Vol. 627, Instrumentation in Astronomy VI. SPIE, Bellingham, p. 733
Tody D., 1993, in Hanisch R. J., Brissenden R. J. V., Barnes J., eds, ASP Conf. Ser. Vol. 52, Astronomical Data Analysis Software and Systems II. Astron. Soc. Pac., San Francisco, p. 173
Traven G. et al., 2017, ApJS, 228, 24
Traven G. et al., 2020, A&A, 638, 145
van de Ven G. et al., 2006, A&A, 445, 513
van der Marel R. P., Anderson J., 2010, ApJ, 710, 1063
Vasiliev E., Baumgardt H., 2021, MNRAS, 505, 5978
Walt S. v. d., Colbert S. C., Varoquaux G., 2011, Comput. Sci. Eng., 13, 22
Wittenmyer R. A. et al., 2018, AJ, 155, 84
Zwitter T. et al., 2018, MNRAS, 481, 645 (Z18)

SUPPORTING INFORMATION

Supplementary data are available at *MNRAS* online.

Table_1a.csv.gz
Table_1b.csv.gz
Table_2.csv.gz
Table_3.csv.gz

Please note: Oxford University Press is not responsible for the content or functionality of any supporting materials supplied by the authors. Any queries (other than missing material) should be directed to the corresponding author for the article.

APPENDIX A: CONTRIBUTIONS OF INDIVIDUAL DATA SETS TO STELLAR MOTIONS WITHIN M 67

In the main text we discuss measurements of stellar motions within M 67 as indicated by observations of *Gaia* and *GALAH+* or *APOGEE* surveys. Here we study contributions of individual data sets by selectively omitting some of the astrometric or spectroscopic measurements.

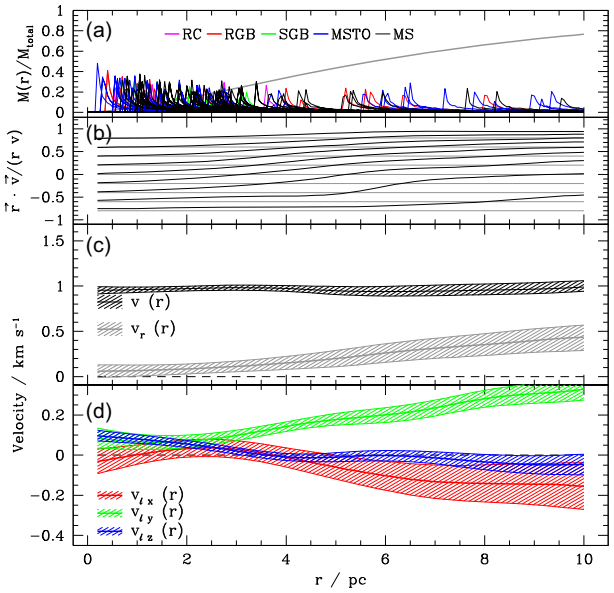

Figure A1. As Fig. 12, but assuming proper motions of all stars are equal to scaled values of the proper motion of the cluster centre: $\mu_{\alpha,\delta} = (d_c/d)\mu_{\alpha,\delta\,c}$. Such a choice emphasizes the role of RV measurements by the *GALAH+* survey and avoids any systematic errors in proper motion measurements, though astrometry is still used to determine the distance distribution of individual stars.

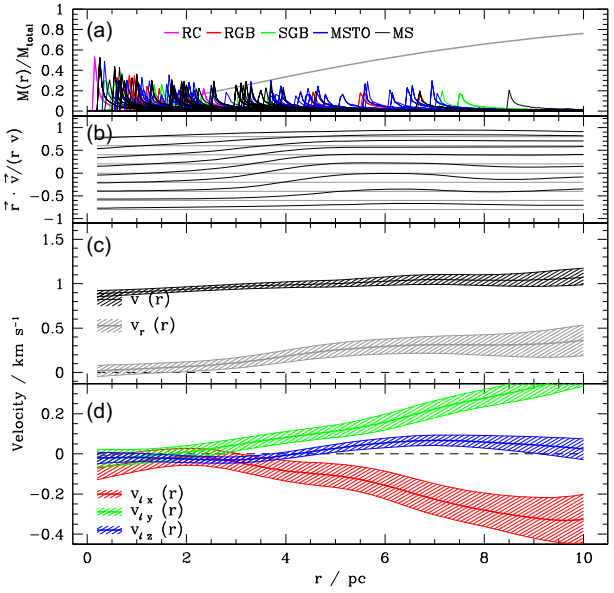

Figure A2. As Fig. A1, but using RVs from the *APOGEE* survey.

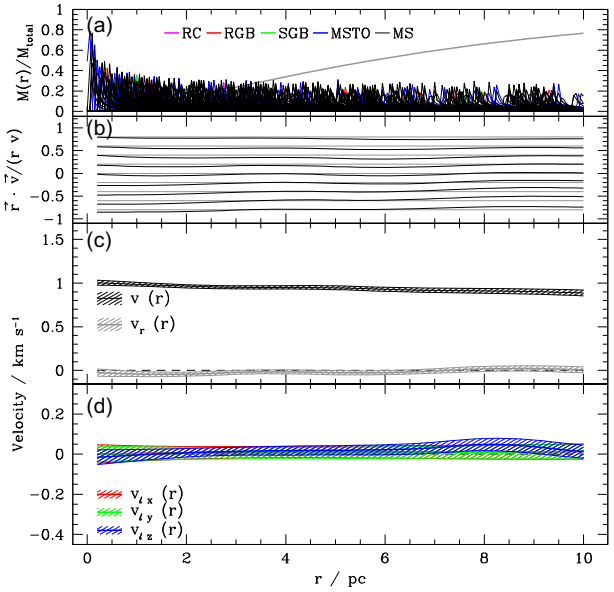

Figure A3. As Fig. 12, but for all stars in *Gaia* eDR3. Since only a small fraction of these stars have RVs measured by *Gaia* and with large error bars we assumed that all stars have their RVs equal to the cluster velocity (RV_c). This assumption lowers the medians of reported velocities and shrinks their error bars.

In Fig. A1, we omit the proper motion information. All stars are assumed to have their proper motions equal to the scaled value of proper motion of the cluster centre: $\mu_{\alpha,\delta} = (d_c/d)\mu_{\alpha,\delta\,c}$. RVs measured by *GALAH+* suggest a radial expansion of the cluster and a rather pronounced rotation in the (x, z) plane. Fig. A2 is an equivalent plot, but using stars with RVs measured by the *APOGEE* survey. Note however that these plots still use some astrometric results from *Gaia*. In particular, parallaxes of individual stars determine the sign of v_r velocities: a star with a RV which is larger than RV_c indicates an

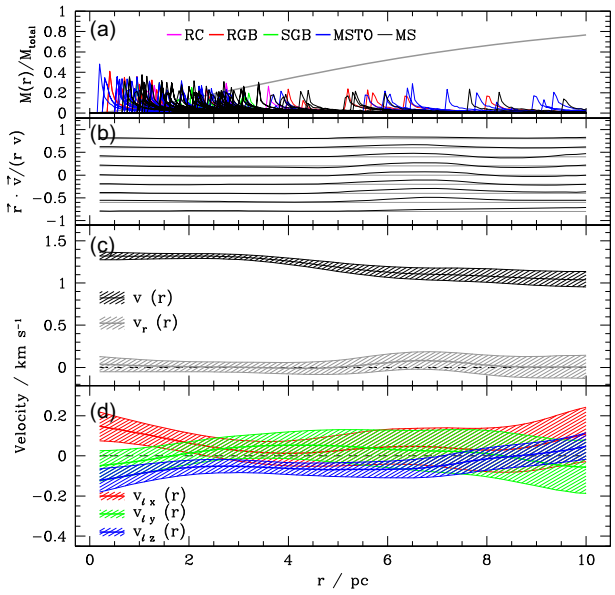

Figure A4. As Fig. 12, but assuming that the velocity vectors of individual stars versus the cluster centre point to random, isotropic directions, while their size is as measured by *GALAH+* and *Gaia*. Average values of v_r and $\vec{v}_\ell$ are not zero because of a small number statistics which reflects a moderate number of M 67 members observed by *GALAH*.

expansion if it lies behind the cluster centre and a contraction if it is located in front of it. Similarly, the value of $v_{\ell y}$ is different for stars which are located further away or closer than the cluster centre.

Fig. A3 uses astrometric information from *Gaia* eDR3 for all cluster members, but omits spectroscopically determined RVs. As explained in the main text, RVs determined by *Gaia* are not sufficiently numerous and accurate for our purpose. So we assumed that all RVs are equal to RV_c. The results are consistent with no internal motions and the error bars are small because of a large number of stars considered. Note however, that the simplistic assumption of constant RVs for all stars is not realistic. Finally we check what happens if we keep the size of the velocity vector of any star with respect to the cluster centre (as measured by *GALAH+* and *Gaia*) but assume its orientation is isotropic (Fig. A4). If the number of stars observed by *GALAH* were large the average motions would be zero. In reality, small number statistics reflects in velocity deviations within the expected uncertainties.

Figs A1 and A2 show that both *GALAH+* and *APOGEE* RVs favour a radial expansion in the outer parts of the cluster which is much more significant than when using measured proper motions of individual stars (Figs 12 and 13). The fact that *Gaia* eDR3 proper motions do not support large scale velocities on the level of 0.1 km s^{-1} or higher is demonstrated by Fig. A3.

[1]*Faculty of Mathematics and Physics, University of Ljubljana, Jadranska 19, 1000 Ljubljana, Slovenia*
[2]*Research School of Astronomy & Astrophysics, Australian National University, Stromlo, ACT 2611, Australia*
[3]*Centre of Excellence for Astrophysics in Three Dimensions (ASTRO-3D), Australia*
[4]*Max Planck Institute for Astrophysics, Karl-Schwarzschild-Str. 1, D-85741 Garching, Germany*
[5]*Sydney Institute for Astronomy, School of Physics, A28, The University of Sydney, Sydney, NSW 2006, Australia*
[6]*Monash Centre for Astrophysics, Monash University, Wellington Rd, Clayton, VIC 3800, Australia*
[7]*School of Physics and Astronomy, Monash University, Wellington Rd, Clayton, VIC 3800, Australia*
[8]*Australian Astronomical Optics, Faculty of Science and Engineering, Macquarie University, Macquarie Park, NSW 2113, Australia*
[9]*Macquarie University Research Centre for Astronomy, Astrophysics & Astrophotonics, Sydney, NSW 2109, Australia*
[10]*Istituto Nazionale di Astrofisica, Osservatorio Astronomico di Padova, vicolo dell'Osservatorio 5, I-35122 Padova, Italy*
[11]*Department of Astronomy, Stockholm University, AlbaNova University Centre, SE-106 91 Stockholm, Sweden*
[12]*Max Planck Institute for Astronomy, Königstuhl 17, D-69117 Heidelberg, Germany*
[13]*School of Physics, UNSW, Sydney, NSW 2052, Australia*
[14]*Stellar Astrophysics Centre, Department of Physics and Astronomy, Aarhus University, DK-8000 Aarhus C, Denmark*
[15]*Department of Physics and Astronomy, Macquarie University, Sydney, NSW 2109, Australia*
[16]*Research Centre for Astronomy, Astrophysics and Astrophotonics, Macquarie University, Sydney, NSW 2109, Australia*
[17]*Institute for Advanced Study, Princeton, NJ 08540, USA*
[18]*Department of Astrophysical Sciences, Princeton University, Princeton, NJ 08544, USA*
[19]*Observatories of the Carnegie Institution of Washington, Pasadena, CA 91101, USA*
[20]*Research School of Astronomy & Astrophysics, Australian National University, Cotter Road, Weston, ACT 2611, Australia also Research School of Computer Science, Australian National University, Acton ACT 2601, Australia*
[21]*Lund Observatory, Department of Astronomy and Theoretical Physics, Box 43, SE-221 00 Lund, Sweden*
[22]*Commonwealth Department of Industry, Science, Energy and Resources, 105 Delhi Road, North Ryde, NSW 2113, Australia*
[23]*Centre for Astrophysics, University of Southern Queensland, Toowoomba, QLD 4350, Australia*

This paper has been typeset from a TEX/LATEX file prepared by the author.